AIAA JOURNAL
Vol. 43, No. 1, January 2005

Effect of Airfoil Aerodynamic Loading on Trailing-Edge Noise Sources

Stéphane Moreau*
Valeo Motors and Actuators, 78321 La Verrière, France
and
Michel Roger†
Ecole Centrale de Lyon, 69134 Ecully, France

A previous experimental investigation of the broadband self noise radiated by an industrial cambered controlled-diffusion airfoil embedded in an homogeneous flow at low Mach number has been extended to various aerodynamic loadings. The instrumented airfoil is placed at the exit of an open-jet anechoic wind tunnel, with a jet width of about four chord lengths. Sound is measured in the far field at the same time as the statistical properties of the wall-pressure fluctuations close to the trailing edge. A new set of mean wall-pressure data has been collected on this airfoil at a chord Reynolds number of 2.9×10^5, which provides some insight on the Reynolds-number effect. Two previously investigated flow regimes with different statistical behaviors are investigated by changing the angle of attack from 8 to 15 deg. They respectively correspond to the nearly separated boundary layer with vortex shedding at the trailing edge and to the turbulent boundary layer initiated by a leading-edge separation.

I. Introduction

In the design process of a new automotive engine-cooling fan system, one major quality factor that has to be fulfilled by Valeo is a minimum noise configuration for a given cooling duty point of a typical module. As mentioned by Caro and Moreau,[1] the noise radiated by this kind of axial machines is both a tonal noise and a broadband noise, both contributions being roughly equal in most configurations. The broadband noise can even be more important in other low-speed axial fans such as the propellers or the blowers of air-conditioning units. An important part of this broadband noise is the fan self-noise generated at the blade trailing edges. According to Wright,[2] this trailing-edge noise also provides the minimum noise that a spinning fan would produce free of any upstream, downstream, and tip interaction.

Trailing-edge noise results from the scattering of turbulent kinetic energy produced in the blade boundary layers into acoustic waves at the geometrical discontinuity of the trailing edge. These turbulent fluctuations and the consequent acoustic pressure fluctuations at an observer position can be obtained numerically for instance, by detailed compressible direct numerical simulations (DNS) or large-eddy simulations (LES). The latter are still hardly achievable even on simplified geometries such as two-dimensional airfoils. To this end, an analytical model has been derived that provides the fan self-noise from a statistical description of the wall-pressure field near the blade trailing edge.[3,4] This model is based on the acoustical analogy and relates the noise power spectral density (PSD) in the far field S_{pp} at a given observer position and for a given frequency, to the power spectral density of wall-pressure fluctuations close to the trailing edge Φ_{pp}, a spanwise correlation length l_y, and an acoustical radiation integral derived from a generalization of the result based on unsteady aerodynamic theories obtained by Amiet.[5,6]

This model was compared by Roger and Moreau[4] with a first set of measurements performed in the Ecole Centrale de Lyon (ECL) small low-speed anechoic wind tunnel on a thin cambered controlled-diffusion (CD) profile developed by Valeo. The mean pressure measurements were compared with detailed Reynolds-averaged Navier–Stokes (RANS) simulations,[7,8] which showed some unprecedented large installation effect. In fact, introducing a loaded airfoil in the stream of an open-jet wind tunnel yields a significant deflection of the jet as a result of the equivalent lateral momentum injection. The net effect is a modified loading on the airfoil with respect to the expected value for the same angle of attack in free air. This motivated the new experiment in the ECL large wind tunnel presented here. The CD airfoil is now placed in a larger 50-cm-wide jet to provide significant airfoil loading change from the previous experiment with a smaller 13-cm-wide jet and validate the RANS numerical model of such experiments developed in Refs. 7 and 8. Both wall-pressure data and far-field noise are compared at the same mean freestream velocity of 16 m/s as the earlier experiment[4] to assess the loading effect. The Reynolds-number effect is also investigated by comparing the results at two different speeds of 16 and 30 m/s. Finally comparisons at two angles of attack, 8 and 15 deg, respectively, provide some insight into two different flow regimes, the turbulent boundary layer, and the vortex shedding, as quoted in Ref. 4.

II. Experimental Setup and Data Collection

As mentioned in Ref. 8, pure airfoil self-noise is better measured by placing the profile in a large quiet environment such as an open-freejet anechoic wind tunnel. The ECL-LMFA (Laboratoire de Mécanique des Fluides et Acoustique de l'Ecole Centrale de Lyon) has two such facilities: a small wind tunnel with dimensions $6 \times 5 \times 4$ m and a nozzle-exit section of 13×30 cm, and a large wind tunnel with dimensions $10 \times 8 \times 8$ m and a nozzle-exit section of 50×25 cm. Previous trailing-edge noise measurements had been done in the smaller anechoic wind tunnel on both the NACA12 and the Valeo CD airfoil. The former provided a validation case against the earlier experiment of Brooks and Hodgson.[9] The latter provided a new set of measurements on an industrial thin and cambered profile with a blunt trailing edge. This family of low-drag airfoils is being used in the latest high-efficiency engine cooling fans designed by Valeo. The corresponding mock-up has a 4% thickness-to-chord ratio and a camber angle of 12 deg. The airfoil chord and span are 13.6 cm (5 in.) and 30 cm (11.9 in.), respectively, fitting the nozzle height. The present experiment has been performed with this same airfoil in the large anechoic wind tunnel. The experimental setup,

Presented as Paper 2003-3225 at the AIAA/CEAS 9th Aeroacoustics Conference, Hilton Head, SC, 12–14 May 2003; received 3 October 2003; accepted for publication 10 August 2004.

*Senior Research Engineer and R&D Manager, Engine Cooling Fan Systems Core Competencies Group. Member AIAA.
†Professor, Laboratoire de Mécanique des Fluides et Acoustique. Member AIAA.

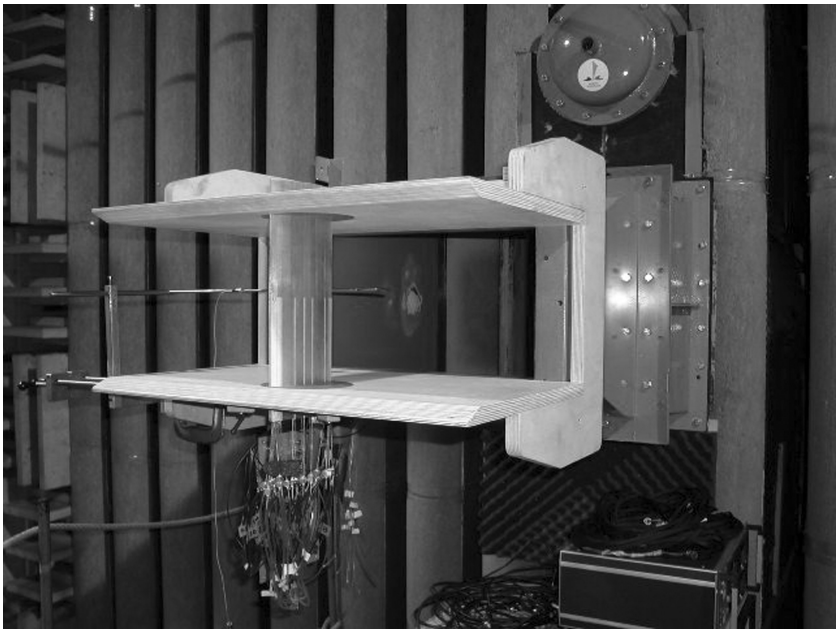

Fig. 1 Experimental setup with the Valeo profile in the ECL test facility.

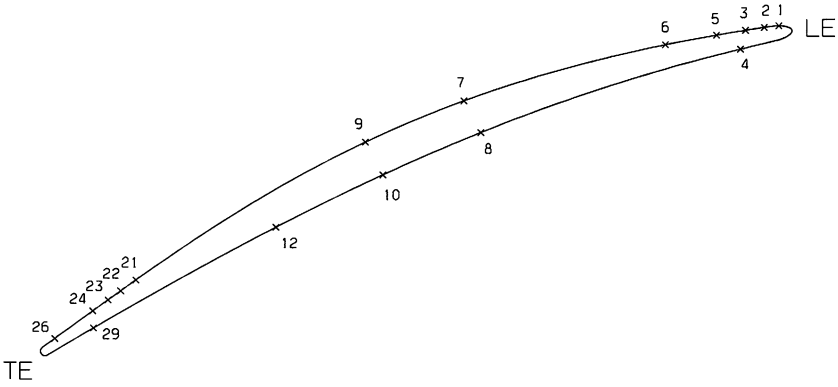

Fig. 2 Sensor locations on the Valeo profile.

shown in Fig. 1, is comparable to that used by Brooks and Hodgson[9] and to the earlier experiment configuration.[8] The geometric angle of attack can be continuously adjusted by two disks rotating inside the side plates around a zero reference aligned with the nozzle outflow. The flow conditions for the CD airfoil are freestream velocities of 16 and 30 m/s, which corresponds to Reynolds number based on the airfoil chord length Re_c of about 1.6×10^5 and 2.9×10^5, respectively. The geometric angle of attack with respect to the chord line has been varied from 8 to 15 deg.

The mock-up[8,10] is equipped with 21 flush-mounted remote microphone probes (RMPs), as shown in Fig. 2. These RMPs[11,12] allow the measurements of both the mean wall-static-pressure and the fluctuating-pressure spectra within the frequency range 20 Hz–25 kHz. Their calibration is made after building the sensor by comparing their response to the equivalent response of a reference B&K 1.27-cm ($\frac{1}{2}$-in.) Type-4181 microphone. Further in situ calibration has been achieved with a B&K Type-4228 pistonphone at 1 kHz. The latter is placed flush mounted on the pinholes of the sensors. Finally movable B&K 1.27-cm ($\frac{1}{2}$-in.) Type-4181 microphones are placed in the far field to collect the acoustic spectra simultaneously. They are mounted at the end of the same traverse, which can rotate around the center of rotation of the mock-up. They are both 2 m distant from the airfoil. Pivoting the traverse allows one to make a directivity plot. The mean static pressure is measured first. All of the PSD data are then collected in two shots with a 16-channel HP3565 Paragon acquisition system. The data of the airfoil front section are first measured, and the data of the airfoil aft part are then acquired. Far-field spectra provide some redundancy between the two consecutive sets of acquisitions. Directivity is then measured automatically by remotely piloting the rotation of the traverse with the two microphones. These simultaneous source and far-field noise data will form a database for the validation of analytical models and direct aeroacoustic simulations.

III. Mean Pressure Measurements

The mean wall-pressure coefficients corresponding to the two selected velocities and incidences are shown in Fig. 3. The measurement uncertainty is less than 0.01 and can be considered as negligible. Yet as in Ref. 8, the sensitivity of the measurements to a maximum variation of angle of attack of 0.5 deg is assessed. It causes a maximum variation of 0.1 on the pressure coefficient in the leading-edge region. They are shown as error bars in Fig. 3 and the consequent pressure coefficient plots. For a geometric angle of attack $\alpha_w = 8$ deg, the flow is attached over most of the chord length, but starts to separate near the leading edge. This can most likely be identified with the laminar flow separations reported by Winklemann and Barlow[13] or Bastedo and Mueller[14] on thin lifting surfaces in low-Reynolds-number flows. This flow regime corresponds to a turbulent vortex shedding with no mean backflow at the

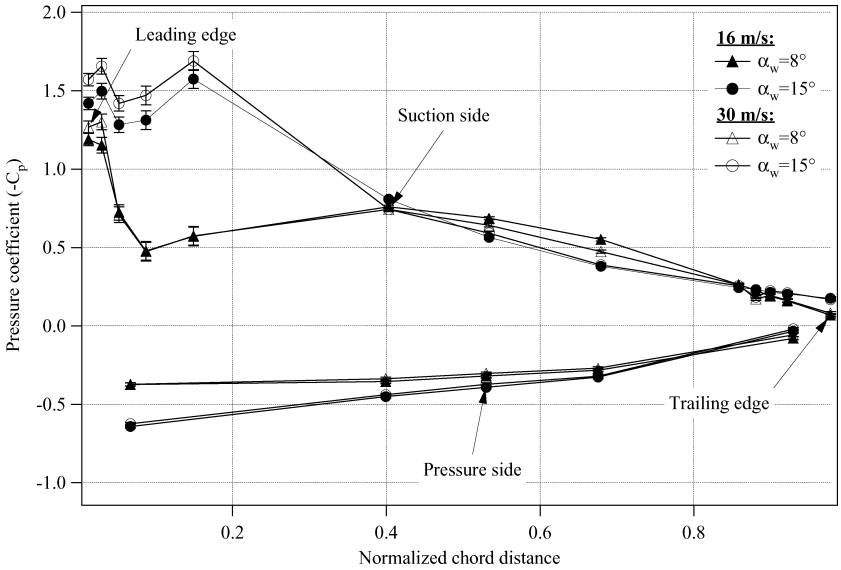

Fig. 3 Comparison of pressure coefficients in the ECL large wind tunnel for two speeds: $U_0 = 16$ m/s ($Re_c = 1.6 \times 10^5$) and $U_0 = 30$ m/s ($Re_c = 2.9 \times 10^5$).

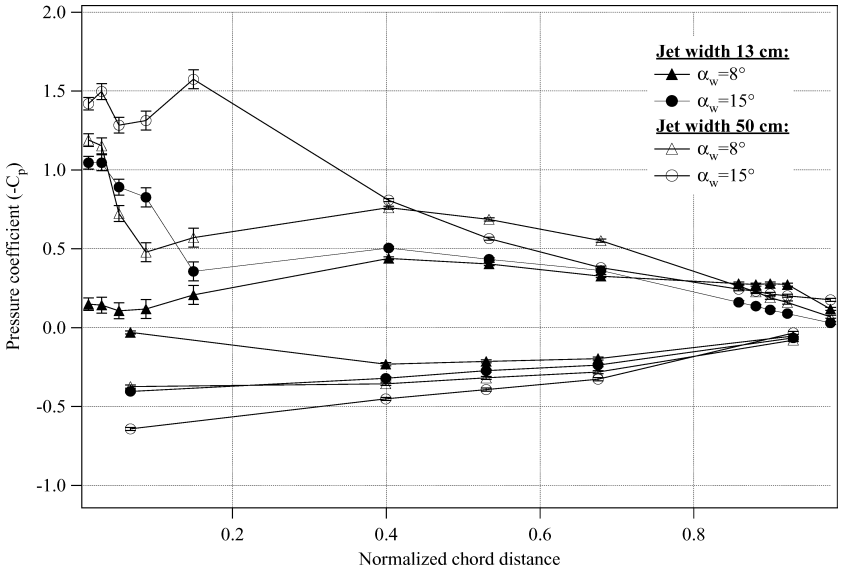

Fig. 4 Comparison of pressure coefficients for two different jet widths.

trailing edge, which was identified below an incidence $\alpha_w = 14$ deg in the previous experiment (Fig. 2 in Ref. 8). Increasing the angle of attack to $\alpha_w = 15$ deg for the large jet width leads to a much larger laminar recirculation that extends far beyond the leading edge. This flow configuration is halfway between the following cases previously investigated in the small anechoic wind tunnel[8]: an incidence of $\alpha_w = 18$ deg, for which a separated zone confined to the leading edge still exists, and the much larger incidence $\alpha_w = 27$ deg, for which the airfoil is completely stalled. This flow regime corresponds to the turbulent boundary layer at the trailing edge previously identifed for angles of attack larger than $\alpha_w = 14$ deg (Ref. 8). Little difference exists between the two flow speeds except at the leading edge in the flow separated zone. Very similar pressure levels are also achieved at the trailing edge for both angles of attack and both speeds.

When comparing the pressure measurements of the two consecutive experiments in Fig. 4 at the same geometric angle of attack, the earlier onset of the laminar flow separation at the leading edge in the large jet width case is obvious. As already noticed, the size of the leading-edge flow separation is almost the same between the larger jet width at the smaller incidence $\alpha_w = 8$ deg and the smaller jet width at the larger incidence $\alpha_w = 15$ deg. Yet, the integrated pressure distribution yielding the lift is larger for the larger jet width at both geometric angles of attack. This result was recently confirmed by accurate RANS simulations of the flowfield around the Valeo CD profile in both ECL wind tunnels.[8] A simplified wind-tunnel model was also used for a parametric study in which the jet width was gradually varied from 13 to 50 cm. Figure 5 shows the good agreement of these latter simulations and the preceding experimental wall-pressure distributions at the angle of attack $\alpha_w = 8$ deg. The wind-tunnel data do not exhibit the large laminar flow separation observed in the free-air case. However, most of the turbulent zone on the suction side for the present large jet width is very close to the free-air case. This good agreement between experimental results and RANS calculations finally suggests that reliable mean flow information for defining the boundary conditions of future LES of trailing-edge noise can be provided by these RANS simulations in the present wide-nozzle case.

IV. Wall-Pressure Statistics

The narrow-bandwidth ($\Delta f = 4$ Hz) PSD Φ_{pp} of the wall-pressure fluctuations are measured with the RMPs just described. The wall-pressure spectra could be reproduced with an accuracy below 1 dB.

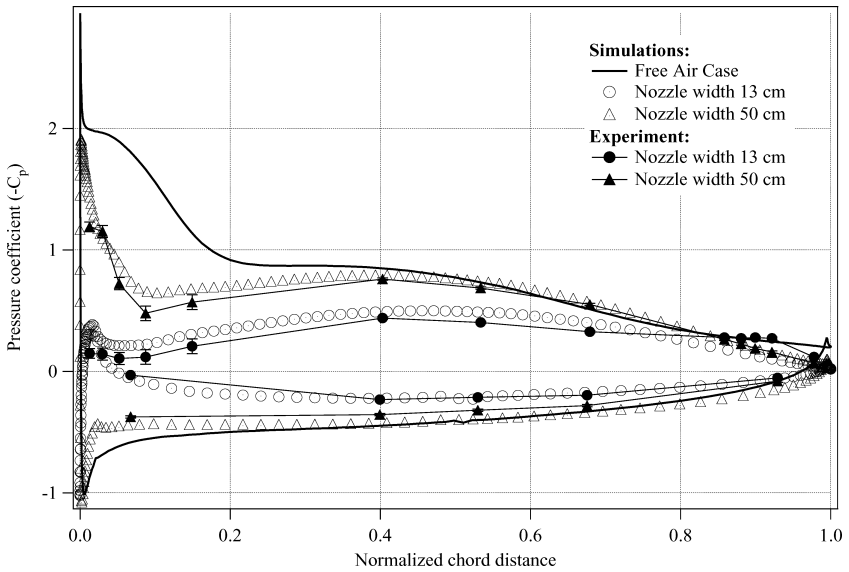

Fig. 5 Comparison of experimental pressure coefficients with RANS simulation at an angle $\alpha_w = 8$ deg.

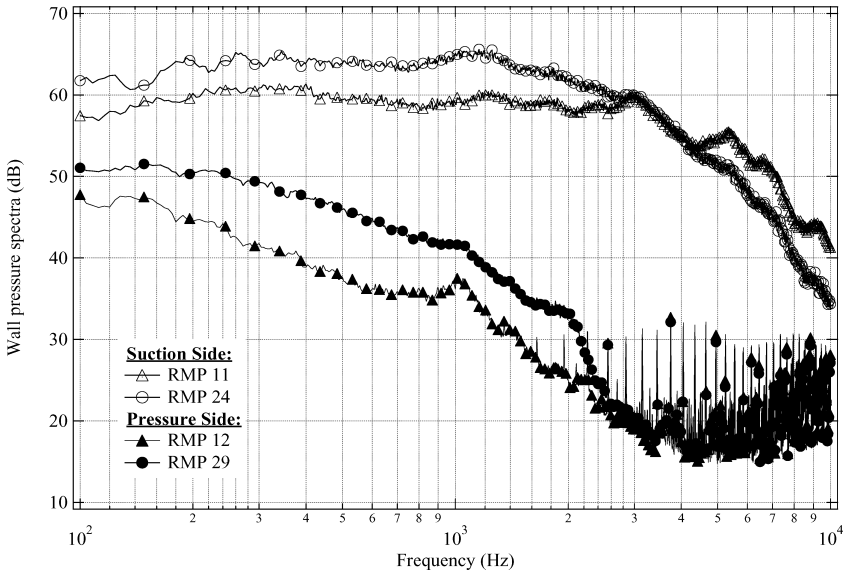

Fig. 6 Comparison of suction-side and pressure-side wall-pressure spectra in the ECL large wind tunnel for $U_0 = 16$ m/s ($Re_c = 1.6 \times 10^5$) and $\alpha_w = 8$ deg.

Reliable and repeatable measurements are achieved for all sensors except at the leading edge (RMPs 1–5) over a range 100 Hz–10 kHz, which is the selected range for all plots.

First, for all flow conditions presently investigated, two very different types of results are obtained on the suction and pressure sides of the airfoil. In Fig. 6, the spectra obtained on two opposite sides at about the same chord location (half the chord length for RMP 11 and 12 and close to the trailing edge for RMP 24 and 19) are compared for a speed of 16 m/s and a geometric angle of attack $\alpha_w = 8$ deg. The pressure-side sensors exhibit much weaker signals than the suction side ones and a different spectral envelope, which indicates a local laminar boundary layer. The pressure-side sensors thus behave as acoustic sensors and measure the near acoustic field from sources presumably located at the trailing edge. In contrast, suction-side RMPs measure true aerodynamic wall-pressure fluctuations, with levels 20 to 40 dB stronger. The acoustic spectra from RMPs 12 and 29 show that sound is essentially radiated at frequencies lower than 3 kHz. The higher-frequency part with sharp peaks most likely corresponds to background noise. Consequently the far-field measurements are only reliable below the 3-kHz limit.

Before comparing the various flow conditions, let us first focus on the reference case considered in Ref. 8 and for which an ongoing LES is performed: a freestream velocity of 16 m/s and an incidence $\alpha_w = 8$ deg. Figure 7 shows very different wall-pressure spectra for all sensors on the front suction side of the airfoil up to RMP 7. This is very similar to the large spectral range (about 50 dB) recently observed by Snarski in the laminar-to-turbulent boundary-layer transition process on a flat plate (Fig. 6a in Ref. 15). Additional narrow spectral features found on RMPs 1, 2, and 3 in Fig. 7 are most likely attributed to the vortex shedding associated with the laminar flow separation. Similar levels and spectral features have been found in the nose region in the recent LES. Moreover, large Φ_{pp} variations have been found on these sensors when repeating the experiment at different times, even though the angle of attack was reproduced with up to 0.25-deg accuracy. Figure 8 shows such large variations for RMP 1. The spectrum corresponding to the circular symbols is almost identical to the behavior observed at RMP 2 in Fig. 7. The spectrum corresponding to the triangular symbols is very similar to both pressure-side spectra in Fig. 6, suggesting a local laminar boundary layer. Both cases stress that a small variation

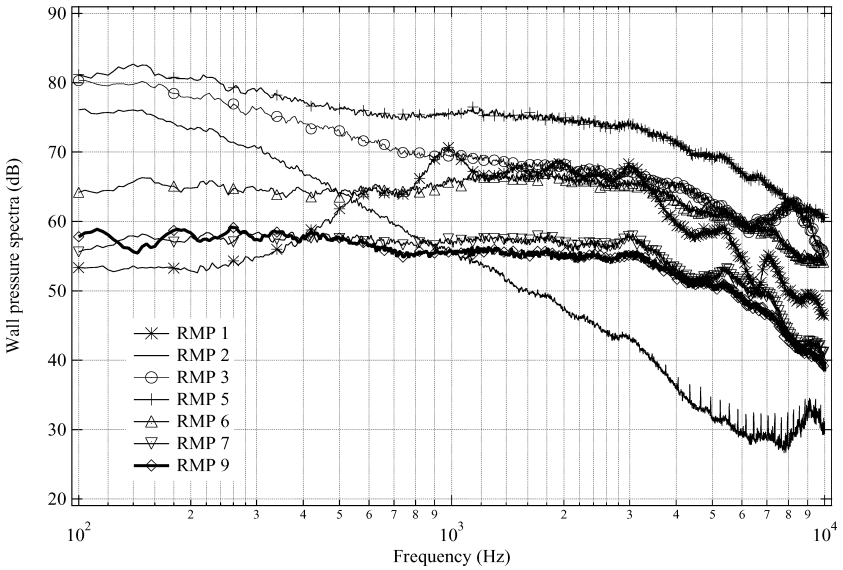

Fig. 7 Streamwise wall-pressure spectra at the front of the airfoil in the ECL large wind tunnel [$U_0 = 16$ m/s ($Re_c = 1.6 \times 10^5$) and $\alpha_w = 8$ deg].

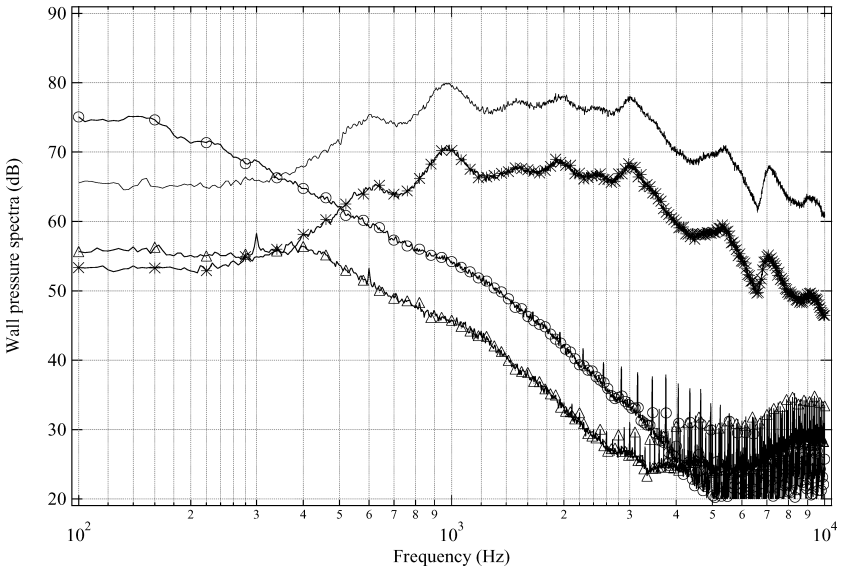

Fig. 8 Comparison of wall-pressure spectra at RMP 1 for repeated experiments in the ECL large wind tunnel [$U_0 = 16$ m/s ($Re_c = 1.6 \times 10^5$) and $\alpha_w = 8$ deg].

of experimental setup (mock-up incidence or freestream flowfield and turbulence level) spatially shifts the onset of the transition and the corresponding spectral features. This confirms the highly intermittent and spatially evolving character of a transitional boundary layer. In Fig. 7, RMP1 can most likely be associated with the onset of the laminar flow separation. The pressure fluctuations then continuously grow up to RMP 5. This sensor always exhibits the largest level for this flow condition and mostly corresponds to a location close to the reattachment point of the preceding laminar flow separation. In the aft portion of the airfoil, the wall-pressure spectra are given for sensors closer to the trailing edge in both streamwise and spanwise directions. Figure 9 represents the wall-pressure spectra in the streamwise direction. The same level and spectral shape is achieved at RMPs 7, 9, and 11, as shown in Figs. 7 and 9. Their location corresponds to the flat portion of the mean pressure distribution shown in Fig. 3. They therefore share similar features to a fully turbulent boundary layer on a flat plate.[16] With the adverse pressure gradient encountered farther downstream, the turbulent boundary layer grows, and the wall-pressure fluctuations increase. Very close to the trailing edge (RMPs 21–26), the wall-pressure statistics is well established and almost stationary justifying the use of radiation models based on a wall-pressure statisitics at a single point close to the trailing edge.[6,17] The spectral homogeneity has also been checked in the spanwise direction. The coherence and phase plots between sensors provide the spanwise correlation length and the local convection speeds respectively. They were obtained by averaging over at least 200 samples in the present experiment. Figure 10 shows the streamwise coherence between all of the pressure side leading-edge sensors and the RMP 5, which is the location of the highest fluctuations. Significant coherence exists not only with the nearest RMP 6 but also with all of the sensors under the laminar flow separation zone experiencing the largest fluctuations. Coherence also has two major frequency features: a regular exponential decay between 100 Hz and 1 kHz similar to the Corcos model for a fully developed turbulent boundary layer over a flat plate and an additional spectral bump centered at 2 kHz. The latter was related to the vortex shedding caused by the laminar flow separation in the first experiment in the small anechoic chamber and was modeled by a Gaussian function in a logarithmic scale.[4] Figure 11 shows the coherence between the suction-side trailing-edge sensors and the RMP 26 in the streamwise direction. It constantly increases with decreasing separation between sensors as expected in a turbulent boundary layer, and all plots mainly exhibit an exponential decay from 100 Hz to 1 kHz. Yet a spectral bump of correlated smaller size structures is still apparent

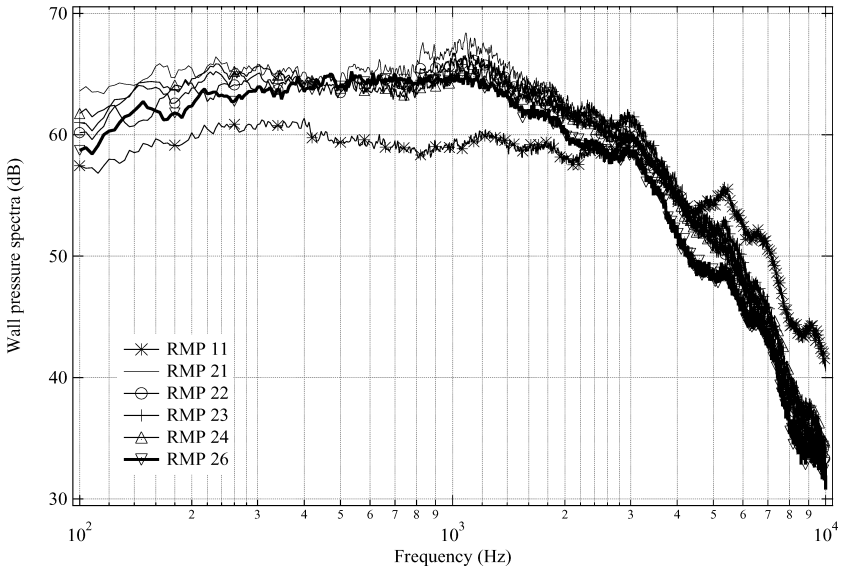

Fig. 9 Streamwise wall-pressure spectra at the aft of the airfoil in the ECL large wind tunnel for $U_0 = 16$ m/s ($Re_c = 1.6 \times 10^5$) and $\alpha_w = 8$ deg.

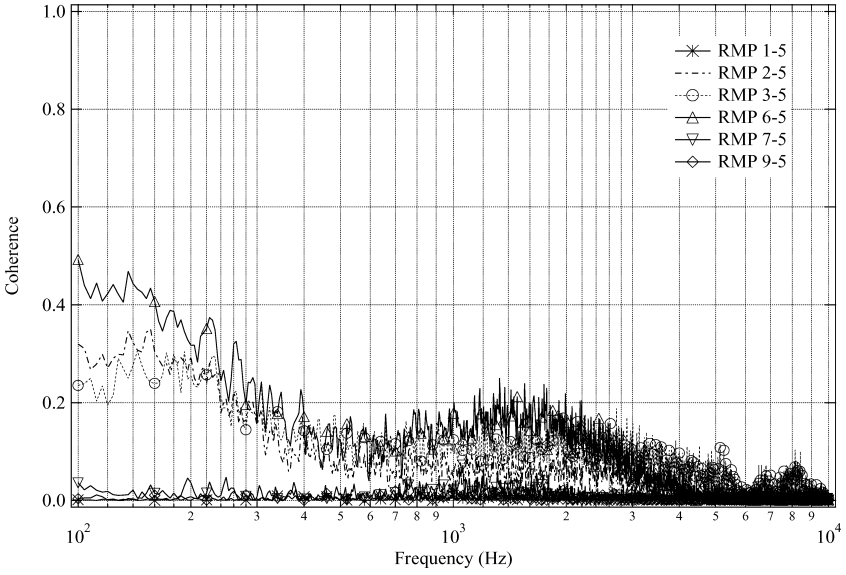

Fig. 10 Streamwise coherence at the front of the airfoil in the ECL large wind tunnel [$U_0 = 16$ m/s ($Re_c = 1.6 \times 10^5$) and $\alpha_w = 8$ deg].

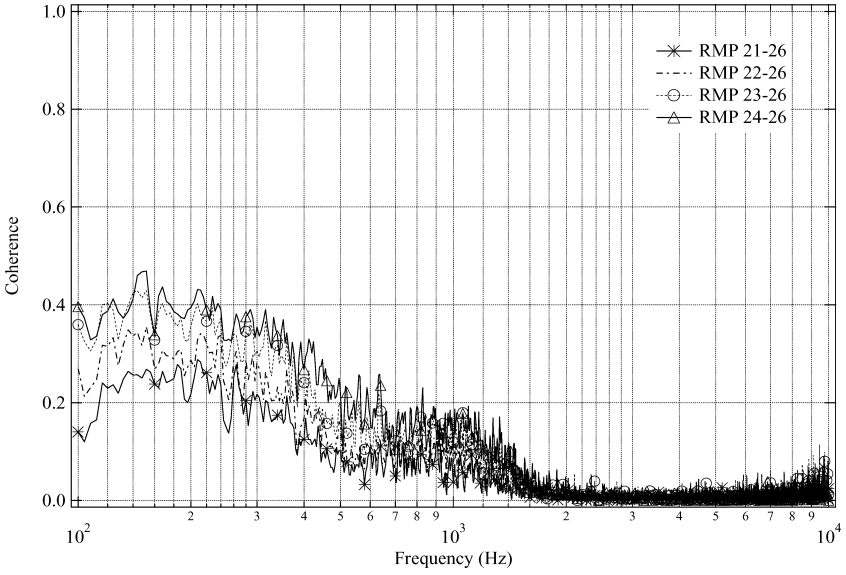

Fig. 11 Streamwise coherence at the aft of the airfoil in the ECL large wind tunnel [$U_0 = 16$ m/s ($Re_c = 1.6 \times 10^5$) and $\alpha_w = 8$ deg].

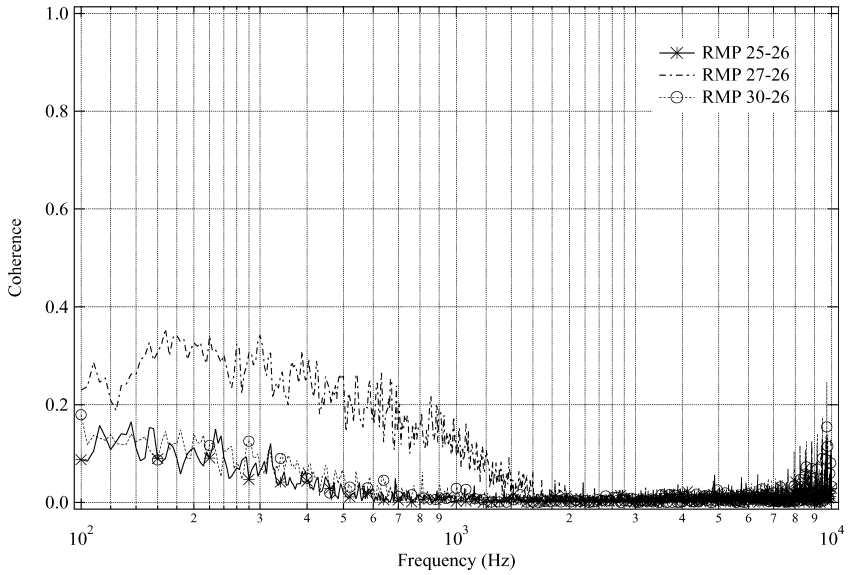

Fig. 12 Spanwise coherence at the aft of the airfoil in the ECL large wind tunnel [$U_0 = 16$ m/s ($Re_c = 1.6 \times 10^5$) and $\alpha_w = 8$ deg].

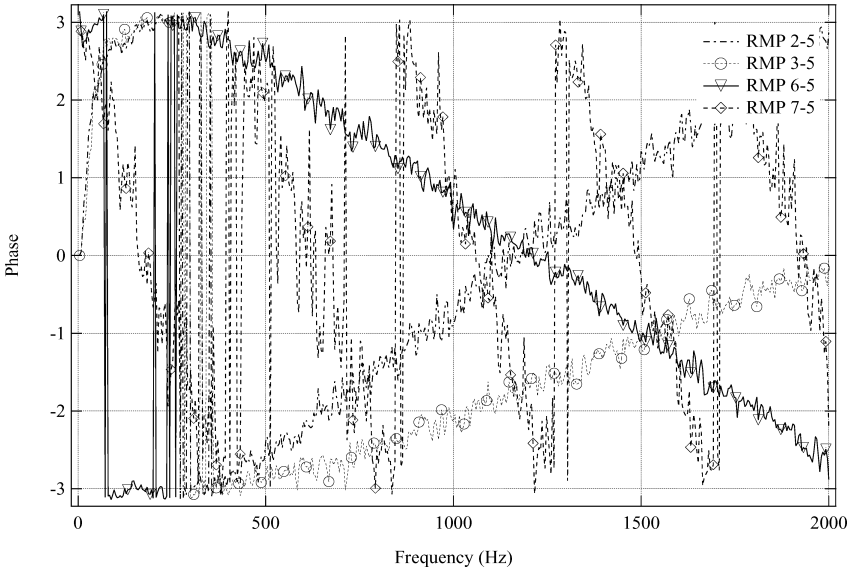

Fig. 13 Phase at the front of the airfoil in the ECL large wind tunnel [$U_0 = 16$ m/s ($Re_c = 1.6 \times 10^5$) and $\alpha_w = 8$ deg].

around 1 kHz. For this frequency range, this feature can be attributed to some similar vortex shedding as for the laminar flow separation at the leading edge. The corresponding coherence plot in the spanwise direction is shown in Fig. 12. The spectral bump centered at about 900 Hz is now larger and has merged with the regular exponential decay at lower frequencies. Figure 13 shows the phase ϕ between most of the suction-side leading-edge sensors and the RMP 5. Clear linear variations are shown for all sensors over ranges $[-\pi, \pi]$ between 0 Hz and 6 kHz, yielding definite convection velocities from the following relationship:

$$U_c = \Delta\omega\Delta\eta/\Delta\phi \tag{1}$$

with $\Delta\eta$ the separation between sensors. Only positive convection velocities are deduced, which further hints at some local downstream vortex shedding rather than at a stationary recirculation bubble as shown in the RANS simulations. The phase plot of RMP 1 yields a highly fluctuating signal with no defined convection speed, which could indicate the onset of the laminar flow separation. In other repeated experiments this signal shifts to RMP 2, which correlates with the previously shown variations of the wall-pressure PSD at the same locations. This is most likely a second evidence of the fluctuating location of the laminar separation zone and its high sensitivity to inlet flow conditions. Figure 14 shows the phase between the suction-side trailing-edge sensors and the RMP 26 in the streamwise direction. They all yield well-defined positive convection speeds, which become about $0.75\,U_0$ at the trailing edge. This is slightly higher than the ratio 0.67 reported for the smaller jet width in Table 1 of Ref. 4.

Figures 15 and 16 compare the wall-pressure spectra measured in the large wind tunnel for the two selected velocities and incidences at the leading edge and at the trailing edge, respectively. The leading-edge results focus on RMP 9 close to the midchord away from the fluctuating flow separation zone to avoid repeatability issues. Very similar spectral shapes are obtained for both speeds suggesting at first sight a small effect of the Reynolds number in this velocity range. As expected at both locations, the levels at 30 m/s are larger, triggering stronger noise sources. For $\alpha_w = 8$ deg, all spectra at RMPs 9 and 26 exhibit three distinct zones. The first one at lower frequencies corresponds to an almost constant PSD. This area extends over at least a thousand hertz for all cases. Beyond a first cutoff frequency at about 1–3 kHz, the overlap region quoted in Ref. 18, which scales as ω^{-1} according to Bradshaw,[19] is observed for RMP 9. The scaling is closer to ω^{-2} for the adverse-pressure-gradient case at RMP 26. Moreover as reported in Ref. 18, the

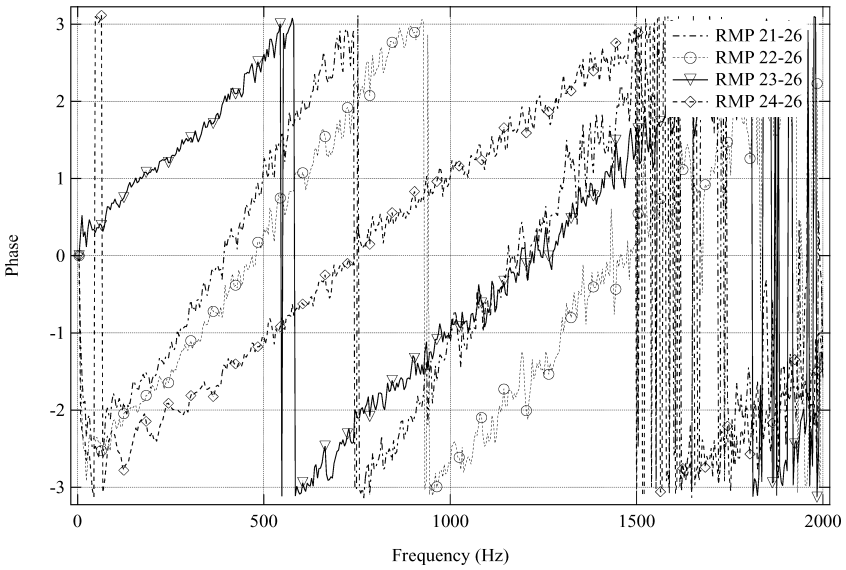

Fig. 14 Phase at the aft of the airfoil in the ECL large wind tunnel [$U_0 = 16$ m/s ($Re_c = 1.6 \times 10^5$) and $\alpha_w = 8$ deg].

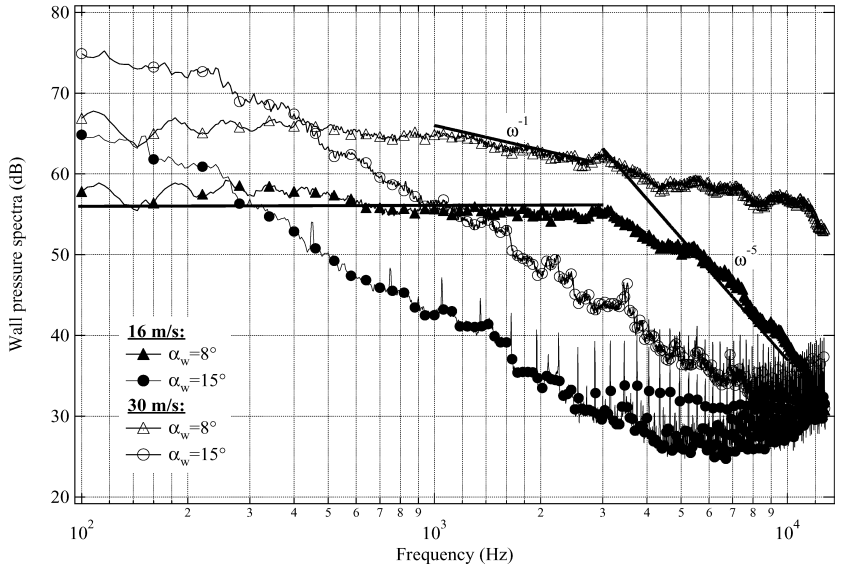

Fig. 15 Comparison of wall-pressure spectra at the leading edge (RMP 9) in the ECL large wind tunnel for two speeds $U_0 = 16$ m/s ($Re_c = 1.6 \times 10^5$) and $U_0 = 30$ m/s ($Re_c = 2.9 \times 10^5$).

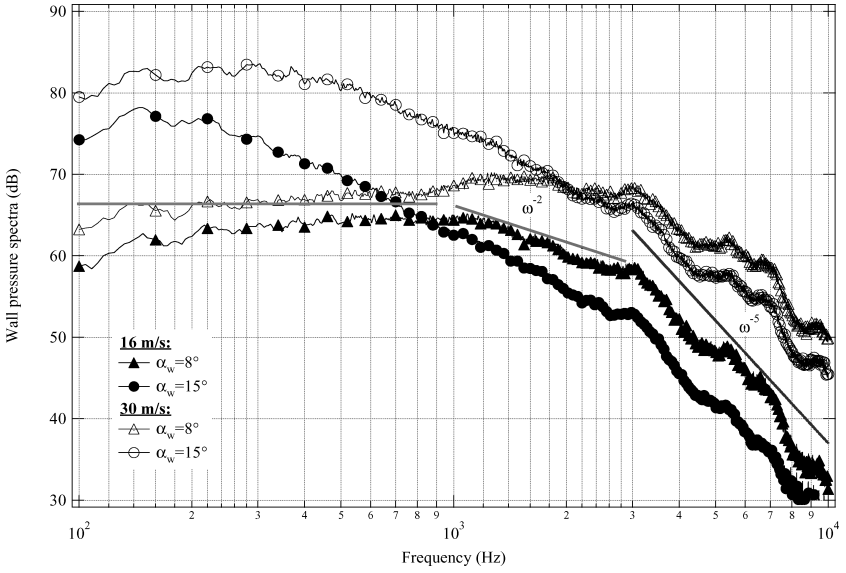

Fig. 16 Comparison of wall-pressure spectra at the trailing edge (RMP 26) in the ECL large wind tunnel for two speeds $U_0 = 16$ m/s ($Re_c = 1.6 \times 10^5$) and $U_0 = 30$ m/s ($Re_c = 2.9 \times 10^5$).

size of this region is increasing with the boundary-layer thickness Reynolds number because of either a higher flow speed or a larger incidence. At high frequencies, after a second cutoff frequency all of the spectra show a decrease with frequencies as ω^{-5}. This typical decay has been postulated and measured beneath two-dimensional and three-dimensional boundary layers[18] for any pressure gradients.[20] At RMP 9, this third zone starts at 5 kHz for 16 m/s and at 10 kHz for 30 m/s. At the trailing edge, the ω^{-5} spectral decay starts at 3 kHz for the lower speed and at about 6 kHz for the higher velocity. These thresholds suggest a scaling with a Strouhal number based on the local suction-side boundary-layer thickness.[4] An additional hump not yet identified is also found at about 3 kHz for all cases at the trailing edge. This, together with small high-frequency oscillations, could be as a result of an imperfect correction for sound-wave attenuation inside the capillary tubes of the RMPs and do not affect the general decreasing behavior. Finally these spectral features suggest that the smooth pressure gradients observed in Figs. 3 and 4, from the transition point triggered by the laminar flow separation up to the trailing edge, are creating flow conditions similar to a two-dimensional developed turbulent boundary layer with mild adverse pressure gradients (local small curvature). These gradients are for instance driving the typical high-frequency content of the wall-pressure spectra.

Figure 17 compares the spectra reported in Ref. 4 for the smaller jet width to the present data. As already found on the mean pressure coefficients, similar results are found for equivalent flow regimes: the lower angles of attack yield spectra typical of the previously described vortex shedding, and the higher angles of attack yield the regularly decreasing spectra with a slope close to -5 almost over the whole frequency range typical of the turbulent boundary layer. Figure 18 compares the coherence at the trailing edge between RMP 27 and RMP 26 for the two selected velocities and incidences. At $\alpha_w = 8$ deg, the low-frequency decay is similar for both speeds, whereas the spectral bump at high frequency is larger and shifted to higher frequencies (around 1800 Hz) for the higher speed. As noted in Fig. 14 of Ref. 4, this is a further hint at a vortex-shedding mechanism, which can be made nondimensional with respect to the preceding Strouhal number. At the largest angle of attack $\alpha_w = 15$ deg, the characteristic exponential decay of a turbulent boundary layer is found. A typical exponential Corcos's model can

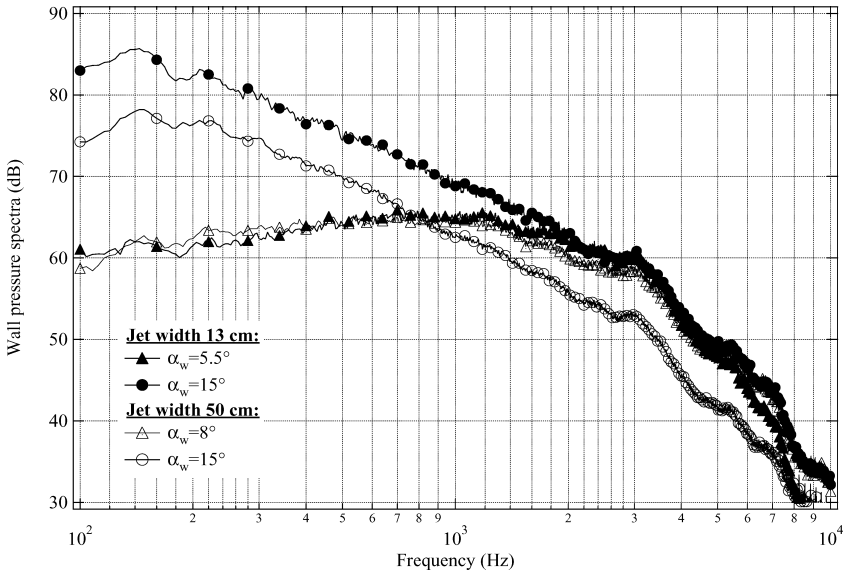

Fig. 17 Comparison of wall-pressure spectra at the trailing edge for two different jet widths.

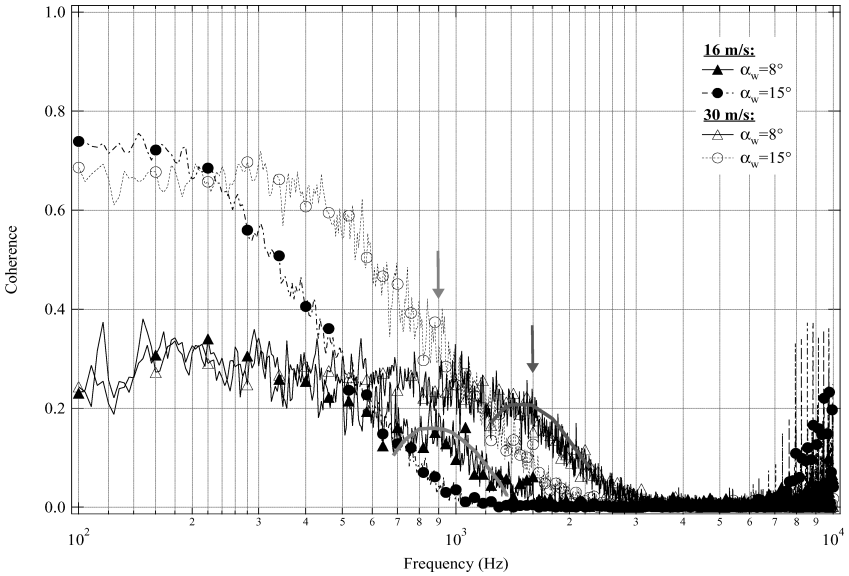

Fig. 18 Comparison of coherence at the trailing edge between RMP 27 and RMP 26 in the ECL large wind tunnel for two speeds $U_0 = 16$ m/s ($Re_c = 1.6 \times 10^5$) and $U_0 = 30$ m/s ($Re_c = 2.9 \times 10^5$).

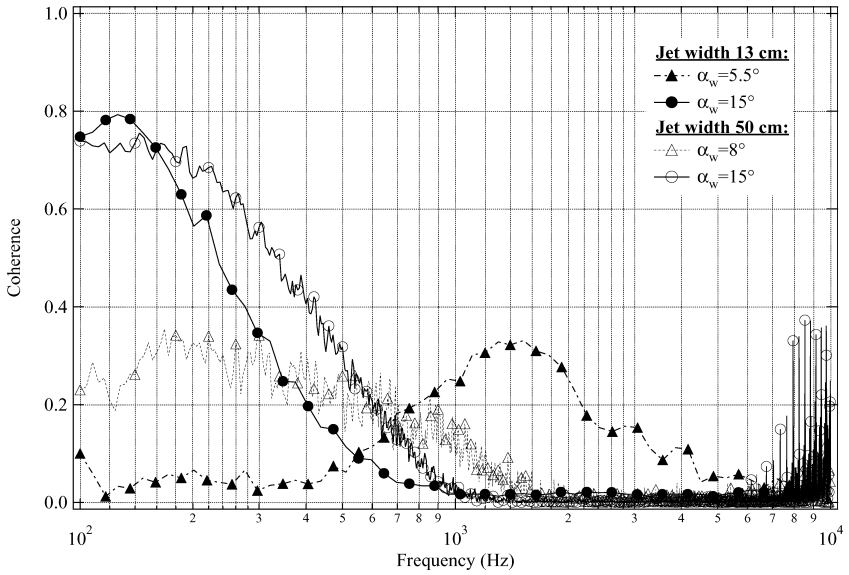

Fig. 19 Comparison of coherence at the trailing edge between RMP 27 and RMP 26 for two different jet widths.

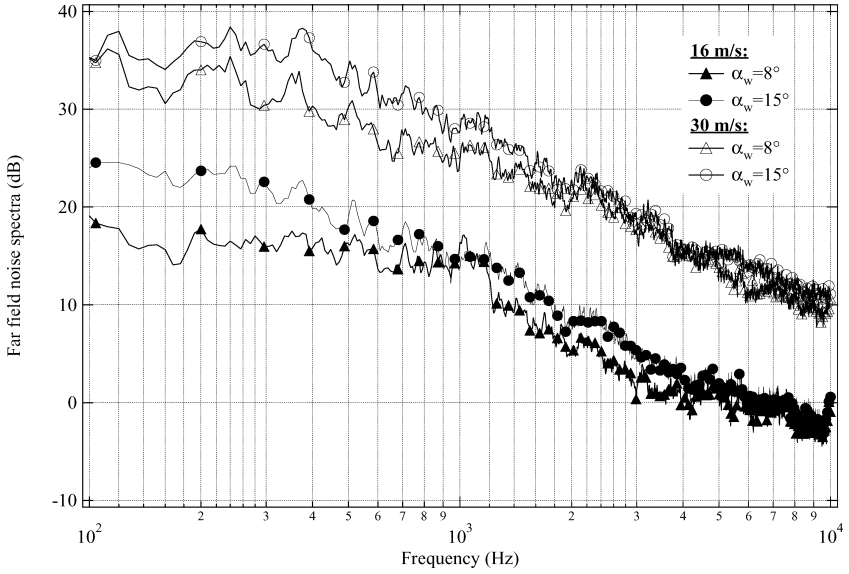

Fig. 20 Comparison of far-field noise spectra in the ECL large wind tunnel for two speeds $U_0 = 16$ m/s ($Re_c = 1.6 \times 10^5$) and $U_0 = 30$ m/s ($Re_c = 2.9 \times 10^5$).

be fitted to this decay for the two speeds (Figs. 20 and 21 in Ref. 10). For the preceding convection velocity at the trailing edge of $0.75\,U_0$, this yields the following spanwise correlation length at the trailing edge:

$$l_y(\omega) = bU_c/\omega \qquad \text{with} \qquad b = 1.2 \tag{2}$$

The constant is slightly smaller than the previously reported $b = 1.5$ in Ref. 4. These different values valid for both speeds on the same airfoil can be caused by different lifts associated with different nozzle widths. The present coherence values are compared to the previously reported smaller jet-width data in Fig. 19. For the lower angles of attack, the magnitude of the high-frequency bump is much larger in the small jet width than in the large one. The associated vortex shedding is much more coherent and dominates any low-frequency mechanism. With the increased jet width, the larger flow structures become more coherent, and the low-frequency exponential decay balances the vortex-shedding hump in the coherence measurements. At $\alpha_w = 15$ deg, the same behavior is observed in the two wind tunnels. The larger jet width triggers a larger flow separation at the leading edge and more coherent vortical structures.

V. Far-Field Measurements

The far-field noise from the Valeo CD airfoil has been measured simultaneously at two opposite angles facing the pressure side and the suction side of the mock-up, using the preceding two B&K 1.27-cm ($\frac{1}{2}$-in.) microphones. The measurement uncertainty is less than 1.5 dB. As in Ref. 4, the background noise has been subtracted to the noise measurements. Typical narrow-bandwidth power spectral densities S_{pp} are given in Fig. 20 for both investigated flow speeds and incidences. Noise frequency and level both increase as flow speed increases. When these PSD are normalized by a fifth power of the freestream velocity U_0^5 and plotted as a function of Strouhal number based on the airfoil chord length in Fig. 21, a good collapse of all previous curves is observed. This emphasizes the noncompact dipolar nature of the trailing-edge noise.[17]

Moreover spectral shapes in Fig. 20 are similar to the corresponding wall-pressure features shown in Fig. 16, with the same frequency

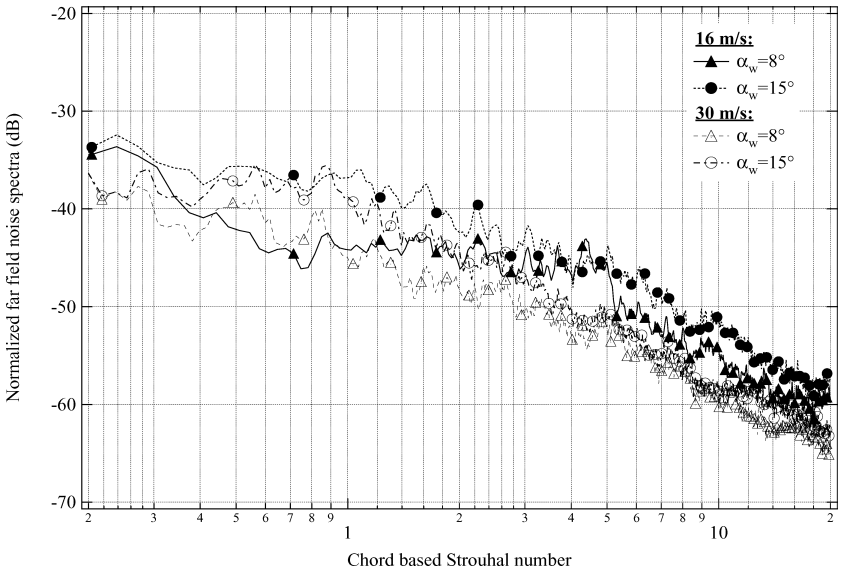

Fig. 21 Comparison of far-field noise spectra in the ECL large wind tunnel normalized by U_0^5 as a function of Strouhal numbers based on the chord length.

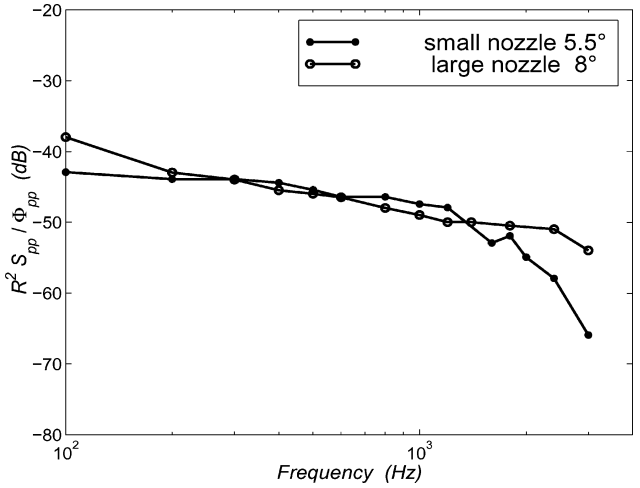

Fig. 22 Transfer function corrected for different distances and span lengths in both experimental setups.

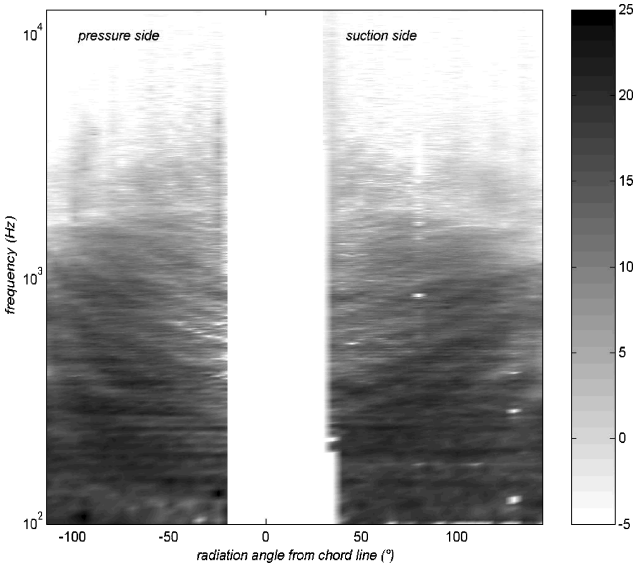

Fig. 23 Typical angle-frequency directivity maps for 15-deg angle of attack: 16 m/s.

crossing between the two incidences at 1 kHz for 16 m/s and 3 kHz for 30 m/s. Figures 24 and 25 in Ref. 10 and Figs. 6, 9, and 12 in Ref. 4 clearly illustrate this fact, suggesting a similar transfer function between the wall-pressure and the far-field noise PSD for similar flow conditions no matter what the jet width might be. This transfer function defined as $R^2(S_{\rm pp}/\Phi_{\rm pp})$, where R is the far-field distance, is shown for the angles of attack 8 deg in the large nozzle case and 5.5 deg in the small nozzle case in Fig. 22. Excellent agreement is found up to 3 kHz, the threshold beyond which the background noise is no longer negligible.

Figure 23 is a typical map of the far-field noise level in the frequency angle of radiation plane. The result stresses that sound is almost symmetrically radiated in half-spaces facing the pressure side and the suction side. This justifies the use of analytical theories[3,4] based on a flat-plate approximation for applications to slightly cambered airfoils. Some inclined patterns of varying directivity with frequency suggest a small interference effect that might be attributed to noncompactness and some spurious diffraction of the sound waves by the edges of the nozzle. A correction procedure is presently in progress to account for this diffraction. Apart from the interference patterns, the map also points out the upstream focusing with increasing frequency, as a specific feature of trailing-edge noise.

VI. Conclusions

The effect of airfoil aerodynamic loading on trailing-edge broadband noise has been investigated experimentally by placing an industrial cambered controlled-diffusion airfoil developed by Valeo in a low-Mach-number jet. Two open-jet anechoic wind tunnels at Ecole Centrale de Lyon have been used to vary the jet width from 13 to 50 cm. The airfoil is placed at the exit of the wind-tunnel nozzle and is instrumented with several remote microphone probes clustered both at the airfoil leading and trailing edges. These sensors have collected a new set of mean wall-pressure data on this airfoil at a chord Reynolds number of 2.9×10^5 and at various angles of attack ranging from 8 to 15 deg. They also measure the power spectral densities of wall-pressure fluctuations. Sound is measured in the far field at the same time as the statistical properties of the wall-pressure fluctuations close to the trailing edge. These various flow conditions provide some insight into the Reynolds-number effect on such an airfoil and into the two previously investigated flow regimes, which correspond to the nearly separated boundary layer with vortex shedding at the trailing edge and to the turbulent boundary layer initiated by a leading-edge separation.

Going to a larger jet width induces a larger lift on the airfoil and an earlier onset of the leading flow separation. The latter is larger at the same angle of attack. It triggers the transition to turbulence and drives up to the trailing edge a wall-pressure statistics similar to a two-dimensional flat plate with mild adverse pressure gradients. Both jet widths still trigger the same overall wall-pressure spectra for equivalent angles of attack and larger levels for the higher speed. Distinct behavior is found between the suction-side and pressure-side sensors. The former behave as areodynamic sensors, the latter as acoustic ones. Large intermittent fluctuations are observed at the leading edge typical of a transitional boundary layer, whereas a very stationary statistics is observed at the trailing in both streamwise and spanwise directions. In all wall-pressure spectra measured from the midchord up to the trailing edge, a distinct ω^{-5} spectral decay is observed, starting at a threshold frequency, which scales with a Strouhal number based on the local suction-side boundary-layer thickness. Yet, the larger jet width induces more coherent large structures in the vortex-shedding flow regime and a slightly modified Corcos statistics in the turbulent boundary-layer flow regime. The latter is characterized at the trailing edge by a larger convection velocity of 0.75 times the freestream velocity and a spanwise correlation length following Corcos's model with a constant of 1.2. In both regimes the transfer function between the wall-pressure spectra and the far-field noise is very similar for both jet widths. This is a further confirmation of the previously developed analytical model of noise radiation based on wall-pressure fluctuations noise sources at the trailing edge.

References

[1]Caro, S., and Moreau, S., "Aeroacoustic Modeling of Low Pressure Axial Flow Fans," AIAA Paper 2000-2094, July 2000.

[2]Wright, S. E., "The Acoustic Spectrum of Axial Flow Machines," *Journal of Sound and Vibration*, Vol. 45, No. 2, 1976, pp. 165–223.

[3]Roger, M., Moreau, S., and Wang, M., "Towards Airfoil Self Noise Prediction Using Wall-Pressure Statistics from LES and an Analytical Acoustic Model," *Center for Turbulence Research Annual Research Briefs*, 2002, pp. 405–414.

[4]Roger, M., and Moreau, S., "Broadband Self-Noise from Loaded Fan Blades," *AIAA Journal*, Vol. 42, No. 3, 2004, pp. 536–544.

[5]Amiet, R. K., "Acoustic Radiation from an Airfoil in a Turbulent Flow," *Journal of Sound and Vibration*, Vol. 41, No. 4, 1975, pp. 407–420.

[6]Amiet, R. K., "Noise due to Turbulent Flow past a Trailing Edge," *Journal of Sound and Vibration*, Vol. 47, No. 3, 1976, pp. 387–393.

[7]Moreau, S., Iaccarino, G., Roger, M., and Wang, M., "CFD Analysis of Flow in an Open-Jet Aeroacoustic Experiment," *Center for Turbulence Research Annual Research Briefs*, 2001, pp. 343–351.

[8]Moreau, S., Henner, M., Iaccarino, G., Wang, M., and Roger, R., "Analysis of Flow Conditions in Free-Jet Experiments for Studying Airfoil Self-Noise," *AIAA Journal*, Vol. 41, No. 10, 2003, pp. 1895–1905.

[9]Brooks, T. F., and Hodgson, T. H., "Trailing Edge Noise Prediction from Measured Surface Pressures," *Journal of Sound and Vibration*, Vol. 78, No. 1, 1981, pp. 69–117.

[10]Moreau, S., and Roger, M., "Effect of Airfoil Aerodynamic Loading on Trailing Edge Noise," AIAA Paper 2003-3225, May 2003.

[11]Pérennès, S., and Roger, M., "Aerodynamic Noise of a Two-Dimensional Wing with High-Lift Devices," AIAA Paper 98-2338, July 1998.

[12]Pérennès, S., "Caractérisation des Sources de Bruit Aérodynamique à Basses Fréquences de Dispositifs Hypersustentateurs," Ph.D. Dissertation in Acoustics, No. 99-32, Ecole Centrale de Lyon, Ecully, France, July 1999.

[13]Winklemann, A. E., and Barlow, J. B., "A Flow Field Model for a Rectangular Platform Wing," *AIAA Journal*, Vol. 18, No. 8, 1980, pp. 1006–1008.

[14]Bastedo, W. G., and Mueller, T. J., "Spanwise Variation of Laminar Separation Bubbles on Wings at Low Reynolds Numbers," *Journal of Aircraft*, Vol. 23, No. 9, 1986, pp. 687–694.

[15]Snarski, S. R., "Wavelet Analysis of Space-Varying Intermittent Wall Pressure Field of Transitional Boundary Layer," American Society of Mechanical Engineers, FEDSM2003-45024 Paper, July 2003.

[16]Keith, W. L., Hurdis, D. A., and Abraham, B. M., "A Comparison of Turbulent Boundary Layer Wall-Pressure Spectra," *Journal of Fluids Engineering*, Vol. 114, No. 3, 1992, pp. 338–347.

[17]Howe, M. S., "A Review of the Theory of Trailing-Edge Noise," *Journal of Sound and Vibration*, Vol. 61, No. 3, 1978, pp. 437–465.

[18]Goody, M. C., and Simpson, R. L., "Surface Pressure Fluctuations Beneath Two- and Three-Dimensional Turbulent Boundary Layers," *AIAA Journal*, Vol. 38, No. 10, 2000, pp. 1822–1831.

[19]Bradshaw, P., "Inactive Motion and Pressure Fluctuations in Turbulent Boundary Layers," *Journal of Fluid Mechanics*, Vol. 30, 1967, pp. 241–258.

[20]Cipolla, K., and Keith, W. L., "Effects of Pressure Gradients on Turbulent Boundary Layer Wave Number Frequency Spectra," *AIAA Journal*, Vol. 38, No. 10, 2000, pp. 1832–1836.

W. Ng
Associate Editor